NACE INTERNATIONAL

CORROSION 2018
Conference & Expo

A Mechanistic Study of the Role of Pyrite in Localized Corrosion of Mild Steel

Jing Ning, Yougui Zheng, Bruce Brown, David Young, and Srdjan Nesic
Institute for Corrosion and Multiphase Technology, Ohio University
342 West State Street, Athens, OH 45701

ABSTRACT

In the previous study by the same authors, a localized corrosion mechanism related to the presence of pyrite corrosion product was proposed by observing and replicating severe localized corrosion in sour environments. In the present study, in order to further validate this localized corrosion mechanism, a comprehensive mechanistic study of localized corrosion was designed and conducted. The experimental design was based on two hypotheses addressing the cause of this type of localized corrosion: an electrochemical galvanic effect and a chemical effect. Thus, novel experiments involving deposition of pyrite particles onto the bare steel surface and onto steel covered by a thin electrically insulating mesh surface were conducted in an aqueous H_2S solution. It was found that no localized corrosion was observed when the physical contact between pyrite particles and the steel underneath was eliminated by using an insulating mesh. Moreover, the experiments were also performed in aqueous CO_2 solution for further validation. Based on the experimental observations, the electrochemical galvanic hypothesis was proven to be the key mechanism in this type of localized corrosion.

Keywords: *Hydrogen sulfide, corrosion, localized corrosion, pyrite, galvanic effect*

INTRODUCTION

The role of a corrosion engineer in the oil and gas industry is to assure integrity and performance of assets through prediction, mitigation, monitoring, and inspection, from casing strings through to the platforms and transportation pipelines, from time of drilling to the time when the field is abandoned. Among many risk factors, localized corrosion of steel is generally considered to be a great risk to asset integrity by causing catastrophic upstream assets failures. On the other hand, it is notoriously difficult to predict, control, and detect localized corrosion, particularly in sour fields. In addition to those practical challenges in the field, the mechanisms and causes of H_2S localized corrosion are unclear. In order to control localized corrosion in sour environments, it is critical to thoroughly understand how it occurs.

The authors' previous experimental study[1,2] has proven that pyrite plays an important role in the initiation of the localized corrosion; however, a more comprehensive mechanistic study on this type of localized corrosion is needed. To bypass the complicated transformation steps between different iron sulfides, pyrite – being a thermodynamically stable iron sulfide, was directly deposited onto the steel surface and the subsequent corrosion process of the steel was studied[2]. Serious localized corrosion

was observed when pyrite particles were deposited onto a mild steel surface in an aqueous H_2S environment, suggesting that the formation of pyrite as a corrosion product in sour environments may initiate localized corrosion. Therefore, it is important to understand the mechanism of this type of localized corrosion caused by pyrite. Moreover, this understanding of localized corrosion can be incorporated into the prediction models of localized corrosion in sour environments.

Two hypotheses were proposed to explain this type of localized corrosion: an electrochemical galvanic effect and a chemical effect. In other words, the localized attack could happen due to a galvanic coupling between the steel and the pyrite layer[3-7] or it may be due to the local water chemistry change (acidification of the solution?) at the steel specimen surface[8] due to the presence of pyrite. In this study, novel experiments were designed and conducted to verify these two hypotheses, and lead to a better understanding of the mechanism of localized corrosion in sour environments caused by pyrite.

EXPERIMENTAL

Experimental Design

Two series of experiments were designed to identify the mechanism of this type of localized corrosion.

> Experimental Series A – testing the hypothesis: localized corrosion is due to a galvanic coupling between pyrite and the mild steel underneath

For this hypothesis to be true, certain basic conditions must be satisfied. These include: the electronic conductivity of pyrite, a physical contact between pyrite and the steel underneath, and the presence of a conductive electrolyte. It is noteworthy that the physical contact between pyrite and steel is one of the preconditions for forming a galvanic coupling, and one which is relatively easy to control in experiments. To that end, experiments were done without and with a very thin insulating mesh introduced between the pyrite particles and the steel sample to avoid physical contact, thereby, eliminating the galvanic coupling between the pyrite deposit layer and the steel sample. Hence, the corrosion process of steel, was investigated in the presence of pyrite being in close proximity to the steel surface so that it could lead to water chemistry changes, but without having galvanic coupling. Table 1 shows the experimental matrix for these experiments. Two experiments were conducted in this series. Experiment #1 is a baseline experiment to reproduce localized corrosion by directly depositing pyrite particles onto steel sample surface with electrical contact. Experiment #2 was done to investigate the mechanism of localized corrosion in the presence of the pyrite particle deposit which was electrically insulated from the steel with a Nylon mesh.

> Experimental Series B: – testing the hypothesis: this type of localized corrosion occurs because of some specific water chemistry (acidification?) caused by the presence of pyrite in a sour environment?

To test this hypothesis, Experimental Series B were set up to prove that this type of localized corrosion can occur even when H_2S is absent, by performing experiments in a pure CO_2 environment. In addition, considering CO_2 gas is ubiquitous in the oil and gas industry, it is of interest to investigate this localized corrosion mechanism in a CO_2 environment. Two separate experiments were completed by depositing silica sand as a "blank" in the first experiment and then pyrite particles in the second experiment, all in an aqueous CO_2 solution.

Table 1 Test matrix for experiments.

Description	Experimental Series A		Experimental Series B	
	Experiment #1	Experiment #2	Experiment #3	Experiment #4
Deposit	Pyrite particles	Pyrite particles + mesh	Silica sand	Pyrite particles
Deposit Particle Diameter	150 ~ 400 µm			
Deposit Layer Depth	2 mm			
Temperature	25 ^{o}C			
Gas Composition	pH_2S (balance with N_2) = 0.1 bar		pCO_2 = 0.97 bar	
Stirring Speed	500 rpm			
Electrolyte	1 *wt.*% NaCl			
Material	API 5L X65			
Experimental Duration	1 week			
Initial pH	4.0			

Apparatus

The under deposit corrosion (UDC) specimen holder used in this study to hold pyrite, is shown in Figure 1 (a). The base, shown on the left with three conductive pins, is designed for easy electrical connection for electrochemical measurements. The specimen holder in the middle is for holding the mild steel specimen, and on the right side the deposit holder shown is used to hold and measure the depth of the deposited particle layer. This assembled UDC setup was exposed to an electrolyte in a glass cell depicted in Figure 1 (b). A stir bar was placed underneath the specimen holder to keep the solution well mixed during the experiment. Figure 1 (b) also shows the elements of an electrochemical cell consisting of a working electrode (abovementioned steel specimen), reference electrode (vs. Ag/AgCl Sat. KCl), and counter electrode (a platinum wire).
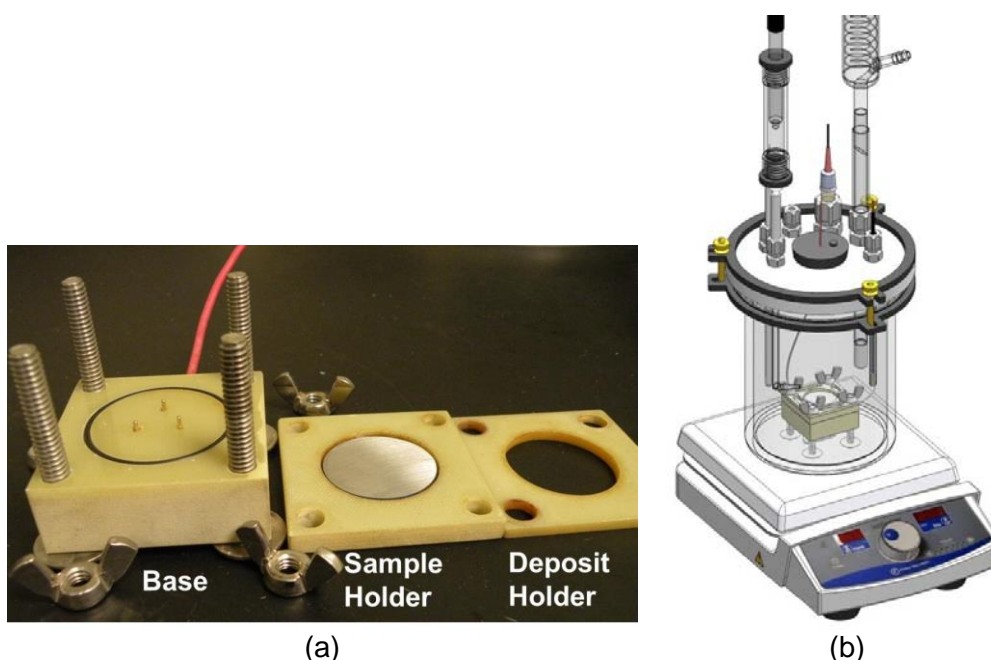

(a)   (b)

Figure 1. (a) UDC specimen holder; (b) Experimental setup.

Materials

Carbon Steel Specifications

Carbon steel specimens with a 7.9 cm^2 exposed area were made from API 5L X65 (UNS K03014) carbon steel. The chemical composition of this carbon steel is shown in Table 2.

Table 2 Chemical composition of X65 carbon steel used in experiment (*wt. %*).

Cr	Mo	S	V	Si	C	Fe	Ni	Mn	P
0.14	0.16	0.009	0.047	0.26	0.13	Balance	0.36	1.16	0.009

Characterization of Deposits

Figure 2 shows scanning electron microscope (SEM) images of the deposits used in experiments. Figure 2 (a) shows the silica sand particles with approximate 150 ~ 400 μm dimensions, and (b) shows pyrite particles of approximately the same size. All deposits were screened using sieves for the desired size.

(a)   (b)
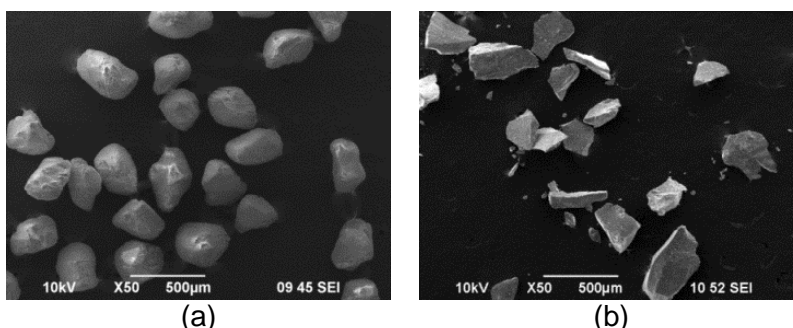
Figure 2. (a) 150~400 μm silica sand;(b) 150~400 μm pyrite particles

A very thin insulating Nylon mesh was used in Experiment #2. Table 3 shows the physical properties of the mesh. Figure 3 (a) shows a SEM image of this insulating mesh, and (b) shows an image of a few pyrite particles with dimensions 150 ~ 400 μm lying on the insulating mesh. Obviously, the physical contact between pyrite particles and the steel sample can be avoided by introducing this insulating mesh; hence the galvanic coupling could be eliminated.

Table 3 Properties of the insulating mesh.

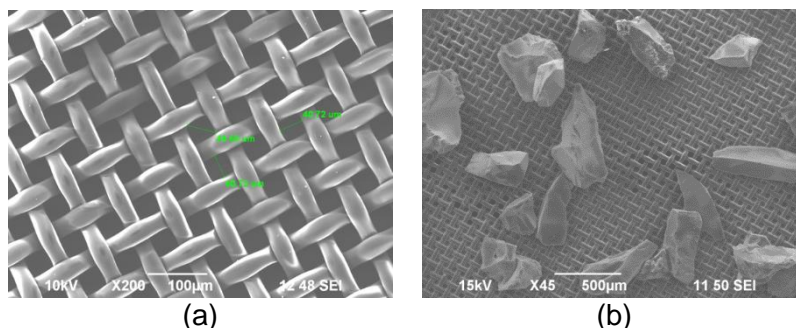| Description	Parameter
Material	Nylon
Opening	41 μm
Open area	33 %
Thickness	60 μm
Diameter	47 mm
pH Tolerance	3 ~ 10
Thermal Stability	up to 180 ^{o}C

Figure 3. SEM image of (a) an insulating mesh; (b) pyrite particles deposited on the mesh

Procedure

Nitrogen gas (N_2) was sparged into the glass cell filled with 2-liter of electrolyte until pH stabilized (typically a few hours). For experiments conducted in a CO_2 solution in Experimental Series B, CO_2 gas was sparged into the electrolyte from the beginning. Bulk pH of the electrolyte was adjusted to pH 4.0 using 1.0 M deoxygenated HCl or NaOH solutions. Deposits (silica sand and pyrite particles) were washed using acetone, rinsed thoroughly with deionized water, blown dry, and put into a container filled with the same electrolyte. The N_2 gas was also sparged into the container until saturated, and the pH of solution in the container was adjusted to pH 4.0 as well.

An API 5L X65 carbon steel specimen with a 7.9 cm^2 exposed area was polished to a 600 grit sand paper finish, rinsed thoroughly with deionized water and isopropanol, ultrasonically cleaned in isopropanol, dried by an air blower, and mounted into the UDC specimen holder as shown in Figure 1. An insulating mesh was used in Experiment #2; Figure 4 illustrates the procedure for introducing the mesh. Then the specimen holder was introduced in the glass cell and the steel specimen was pre-corroded for one hour. A 2 mm thick layer of silica sand or pyrite particles was deposited onto the steel specimen surface. An H_2S and N_2 mixed gas with 10% H_2S in the gas phase was sparged into the glass cell approximately one hour after the deposition of the solid layer. The experiment lasted a full week in order to be able to detect any initiation of localized corrosion. Electrochemical measurements on the steel specimen were conducted to obtain the general corrosion rate of the steel specimen and the solution resistance using a Gamry[‡] Reference 600 Potentiostat. After the experiment, SEM and energy dispersive X-ray spectrometry (EDX) were used to analyze the surface morphologies of the steel specimen. In addition, weight loss of the steel specimen was performed to confirm the B value used for linear polarization resistance (LPR) measurements. Surface profilometry of the specimen after removing the corrosion product layer was performed confirming the occurrence of localized corrosion.
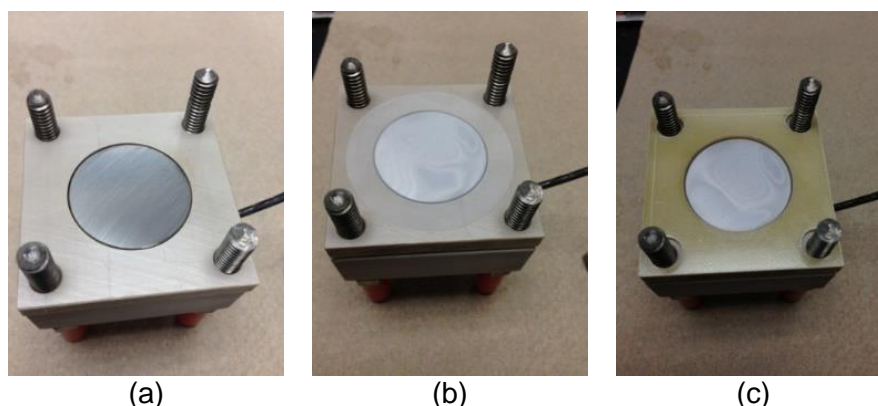

Figure 4. Procedure for introducing the insulating mesh: (a) a steel sample prepared and introduced into the sample holder; (b) a non-conductive mesh used over the sample surface; (c) the deposit holder placed over the mesh.

EXPERIMENTAL RESULTS

Experimental Series A

General Corrosion Rate and Open Circuit Potential (OCP)

Evolution of OCP and corrosion rate in the initial five hours of Experiment #1 including the deposition of a pyrite particle layer and the introduction of H_2S gas are shown in Figure 5. A large increase in both the OCP and corrosion rate was observed after the deposition of the pyrite particle layer. This is thought to be due to the contact of steel with the more noble pyrite and possibly due to a significant increase in the rate of cathodic reaction(s) in the presence of pyrite deposits.

After H_2S gas was introduced, both OCP and corrosion rate increased dramatically, which was due to the addition of one more cathodic reaction species – aqueous H_2S. The OCP and corrosion rate throughout the experiment lasting a week are shown in Figure 6. The general corrosion rate was stable throughout the experiment. WL corrosion rate result shown as a green diamond on the right side of Figure 6 agreed well with LPR measurements using a B value of 13 mV. Solution pH was also monitored throughout the experiment, which was found to increase to 4.7 after 2 days of exposure and it was stable through the remainder of the experiment.
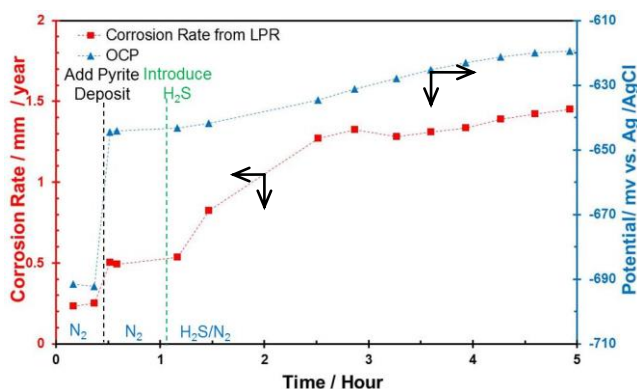
Figure 5. Corrosion rate and OCP using pyrite particle in the initial hours of Experiment #1 (2 mm thick pyrite particles deposit layer, $pH_2S = 0.1bar$, initial pH 4.0, T = 25°C).
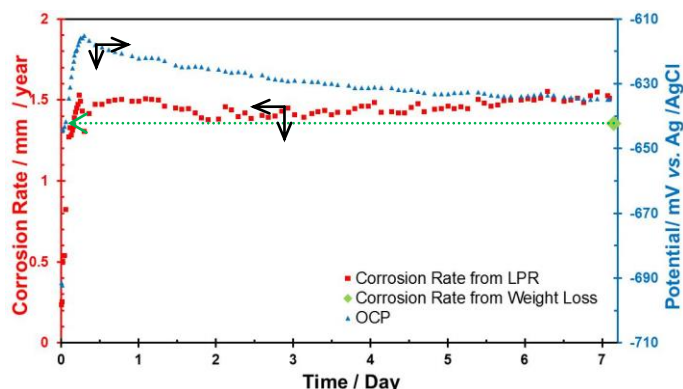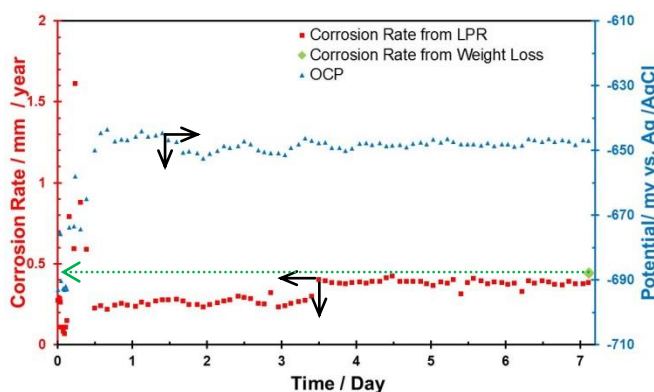

Figure 6. Corrosion rate and OCP using pyrite particle deposit for a week in Experiment #1 (2 mm thick pyrite particles deposit layer, $pH_2S = 0.1bar$, initial pH 4.0, T = 25°C).

Figure 7 shows the change of OCP and corrosion rate in the presence of a very thin nylon mesh separating the pyrite layer from the steel, over the initial six hours, including the steps of the deposition of pyrite particles and the sparging of H_2S gas to the solution. A decrease in both OCP and corrosion rate after the deposition of pyrite particles was observed, in contrast to the large increase in both OCP and corrosion rate which was seen without using the insulating mesh, as shown in Figure 5. Hence, it

can be concluded that the increase in OCP and corrosion rate after the deposition of pyrite in the previous Experiment #1 was due to the galvanic effect and not because of a surface water chemistry change cause by pyrite. This does not come as a surprised when one considers that pyrite is one of the most stable iron sulfides and was unlikely to dissolve and alter the surface water chemistry. This experiment was conducted for a week, and OCP and corrosion rate throughout experiment are shown in Figure 8. Comparing with the corrosion rate shown in Figure 5, a significant decrease in corrosion rate was observed by using this mesh. In addition, WL corrosion rate result confirmed LPR measurements. A slight and slow increase in solution pH, from the initial pH 4.0 to pH 4.8 on the 7th day, was observed during this experiment.
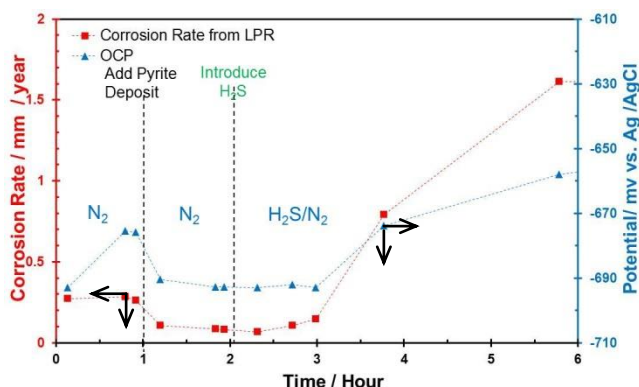
Figure 7. Corrosion rate and OCP with pyrite particles deposited on the mesh in the initial hours of Experiment #2 (Nylon mesh, 2 mm thick pyrite particles deposit layer, pH$_2$S = 0.1bar, initial pH 4.0, T = 25 ^{o}C).

Figure 8. Corrosion rate and OCP with pyrite particles deposited on the mesh for a week in Experiment #2 (Nylon mesh, 2 mm thick pyrite particles deposit layer, pH$_2$S = 0.1bar, initial pH 4.0, T = 25 ^{o}C).

Comparison of Surface Morphologies

Surface morphology of the specimen after the removal of the pyrite particle deposit layer and the associated corrosion product layer in Experiment #1 is shown in Figure 9, from which severe localized corrosion features can be observed. A number of locations with pitting corrosion found on the steel specimen are shown at higher magnification in Figure 10. The number on the upper left corner of each SEM image in Figure 10 indicates the maximum diameter of the pit. However, by introducing the insulating mesh in Experiment #2, a featureless flat surface with no localized attack was observed, shown in Figure 11 after the removal of the pyrite deposit, insulating mesh, and corrosion product layers.

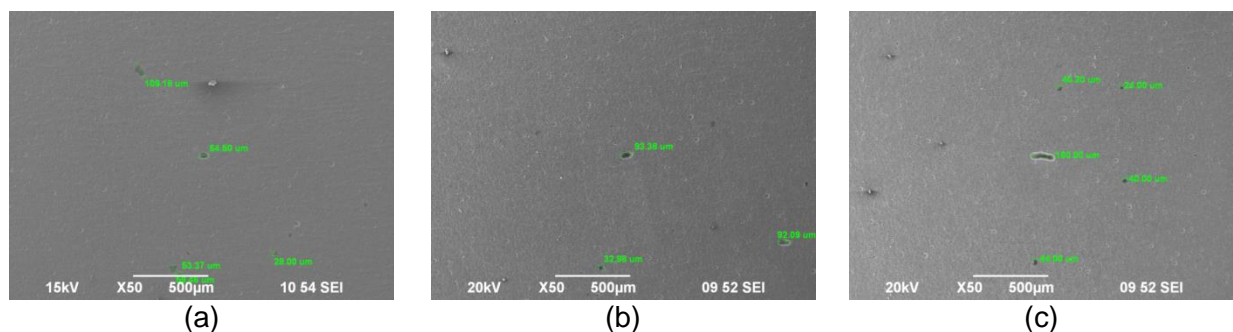(a)   (b)   (c)

Figure 9. Surface morphologies of the specimen at different locations after removing the corrosion product layer using pyrite particle deposit in Experiment #1(2 mm thick pyrite particles deposit layer, $pH_2S = 0.1bar$, initial pH 4.0, T = 25°C).
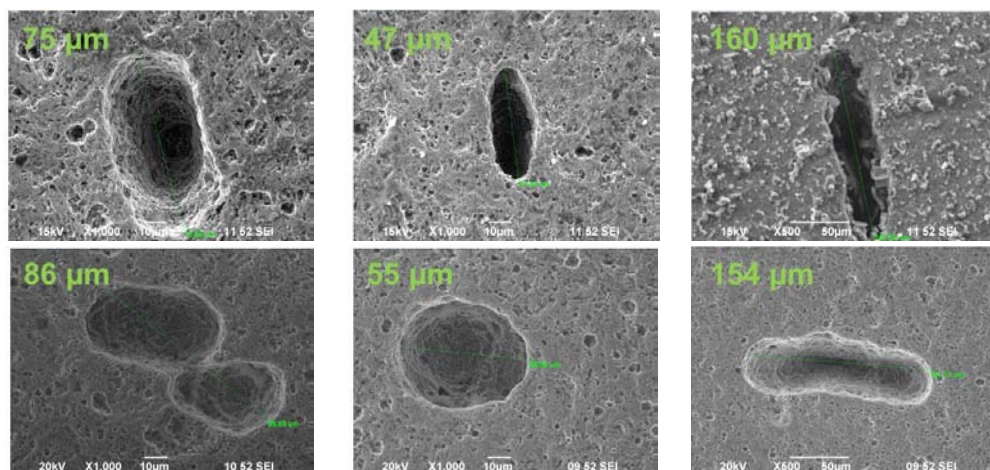

Figure 10. Locations of localized corrosion on the specimen using pyrite deposit in Experiment #1 (2 mm thick pyrite particles deposit layer, $pH_2S = 0.1bar$, initial pH 4.0, T = 25°C).
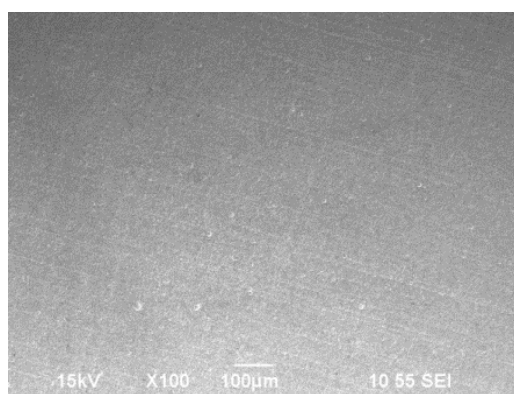
Figure 11. Surface morphology of the specimen after removing corrosion product layer using pyrite particles deposited on the nylon mesh in Experiment #2 (Nylon mesh, 2 mm thick pyrite particles deposit layer, $pH_2S = 0.1bar$, initial pH 4.0, T = 25°C).

After removing the corrosion product layer, some areas on steel specimens were arbitrarily selected for profilometry analysis to reveal any additional features across the surface. Profilometry of the specimen which has no nylon mesh is shown in Figure 12 (a) and the maximum pitting depth, 135 µm, found on the specimen is shown in Figure 12 (c). Profilometry of the steel sample in the presence of the nylon mesh is shown in Figure 12 (b), and the maximum "localized" corrosion depth, 9 µm, found on this specimen (this is considered to be an inclusion) is shown in (d). Accordingly, it can be concluded that no localized corrosion was observed by using the insulating nylon mesh.

Figure 13 shows a comparison of general and localized corrosion rates between Experiment #1 and Experiment #2. The general corrosion rate was obtained from weight loss results, and the maximum localized corrosion rate was converted from the maximum pitting depth. The time averaged pit penetration rate was up to 7 mm/year during the 7 days of exposure in the presence of pyrite particle layers in Experiment #1. However, when the physical contact between pyrite particles and the steel underneath was eliminated using an insulating nylon mesh, no localized corrosion was observed in Experiment #2. Thus, the electrochemical galvanic coupling hypothesis was proven to be the valid in this type of localized corrosion.

(a)	(b)
(c)	(d)
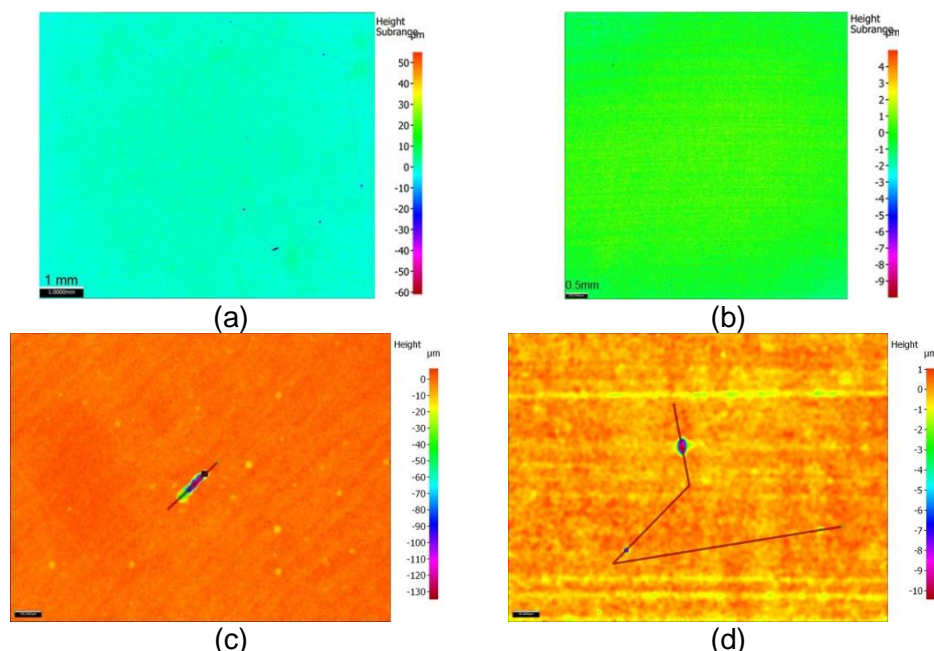
Figure 12. (a) Profilometry feature with pyrite deposit in Experiment #1; (b) Profilometry feature with pyrite particles deposited on mesh in Experiment #2; (c) Maximum pit depth in Experiment #1; (d) Maximum pit depth in Experiment #2.
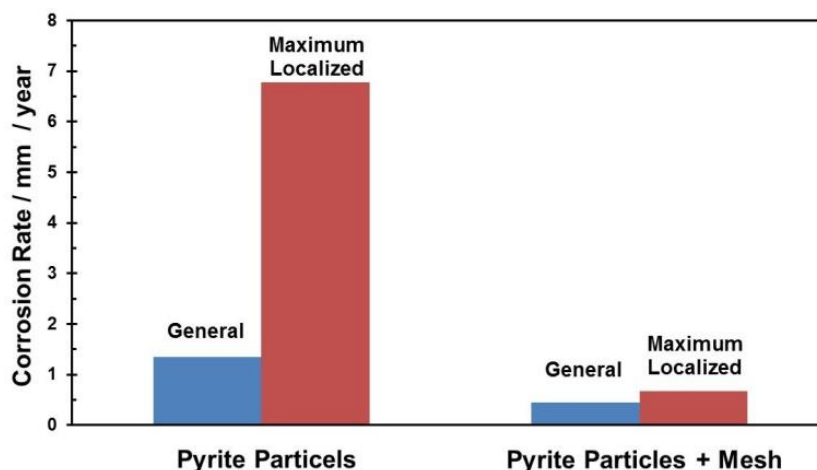

Figure 13. Comparison of corrosion rates between without mesh and with mesh.

Experimental Series B

General Corrosion Rate and Open Circuit Potential

Corrosion rate was retarded after the deposition of the silica sand layer in Experiment #3, as shown in Figure 14, and it was then stable through the remainder of the experiment, as shown in Figure 15. It is understood that the decrease in corrosion rate is due to the blockage effect by the porous sand deposit. A stable solution pH was observed in this experiment of 7 days due to the low corrosion rate, which was pH 4.5 at the end of this experiment.

In Experiment #4, a decrease in corrosion rate and an increase in OCP were observed after the deposition of pyrite particles in Figure 16. OCP and corrosion rate were stable throughout Experiment #4 for a week, as shown in Figure 17. Corrosion rate did not increase immediately after the deposition of pyrite particles in Experiment #4 conducted in a CO_2 solution such as was the case in Experiment #1 performed in an aqueous N_2 and then H_2S/N_2 environment. It is believed that this is due to different corrosion mechanisms associated with sour/sweet corrosion. In the N_2 and H_2S/N_2 solution in Experiment #1, the corrosion process of the specimen was under diffusion control. The deposition of pyrite particles onto specimen surface provided more cathodic reaction area. Thus, the species for cathodic reactions such as H^+ did not necessarily need to diffuse to the specimen surface for cathodic reactions to occur, and happened at the pyrite surface instated. Therefore, an increase in cathodic reaction was observed in Experiment #1. However, Experiment #4 was conducted in a CO_2 solution, in which the corrosion process of specimen was dominated by CO_2 hydration, a chemical reaction. This hydration reaction was not enhanced by deposition of pyrite particles. Moreover, the deposition of pyrite particles retarded general corrosion rate due to a blockage effect. Hence, a decrease in the general corrosion rate after deposition of pyrite particles was observed in a CO_2 solution as shown in Figure 15 and Figure 16. Solution pH was monitored throughout the experiment for 7 days. An increase in pH was seen, which was pH 4.7 at the end of this experiment.

However, the WL corrosion rate of Experiment #4 in the presence of pyrite particles, 0.6 mm/year, was accelerated compared to the WL corrosion rate of Experiment #3 with silica sand, which is 0.3 mm/year. This indicates that pyrite particles did not act entirely as inert silica sand particles did; it is assumed that pyrite layer caused a galvanic coupling as they did in an H_2S solution and contributed to a higher WL corrosion rate.
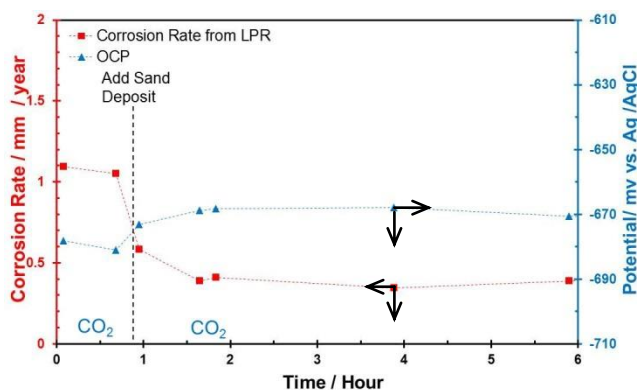

Figure 14. Corrosion rate and OCP using silica sand deposit in a CO_2 solution in the initial hours of Experiment #3 (2 mm thick silica sand deposit layer, pCO_2 = 0.97bar, initial pH 4.0, T = 25 $^{\circ}$C).
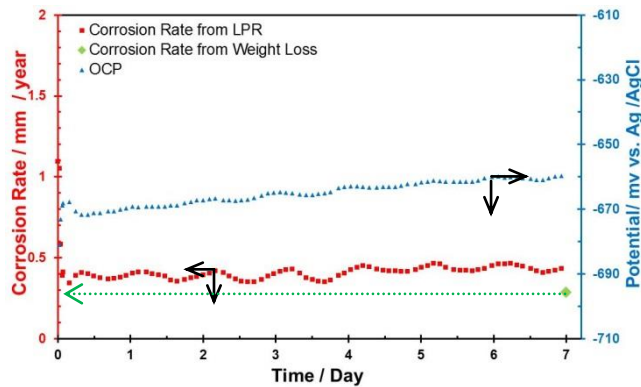
Figure 15. Corrosion rate and OCP using silica sand deposit in a CO_2 solution for a week in Experiment #3 (2 mm thick silica sand deposit layer, pCO_2 = 0.97bar, initial pH 4.0, T = 25 ^{o}C).

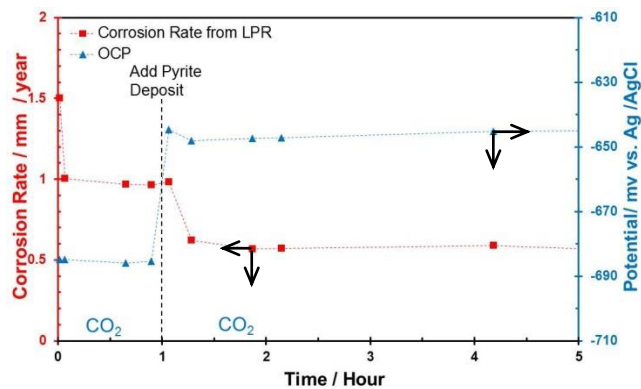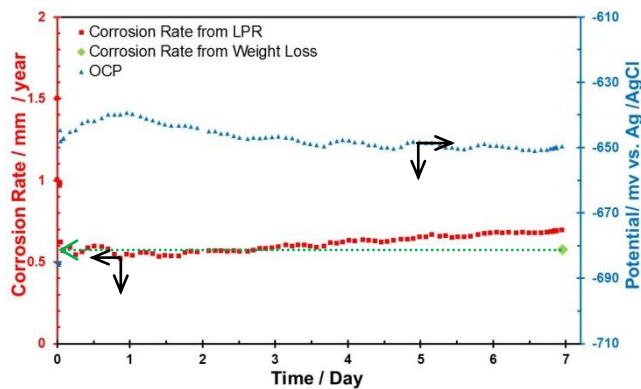

Figure 16. Corrosion rate and OCP using pyrite particle deposit in a CO_2 solution in the initial hours of Experiment #4 (2 mm thick pyrite particles deposit layer, pCO_2 = 0.97bar, initial pH 4.0, T = 25 ^{o}C).

Figure 17. Corrosion rate and OCP using pyrite particle deposit in a CO_2 solution for a week in Experiment #4 (2 mm thick pyrite particles deposit layer, pCO_2 = 0.97bar, initial pH 4.0, T = 25 ^{o}C).

Comparison of Surface Morphologies

The corrosion product layer on the specimen was removed to reveal the corroded steel surface. Figure 18 shows surface morphologies of the specimen in Experiment #3 in the presence of silica sand. The original steel surface with polishing marks was still seen at a few locations where silica sand occupied the steel surface. It reveals that the silica sand deposited on the steel surface protected the steel underneath from the corrosive environment due to a blockage effect. Figure 19 shows surface morphologies of the specimen in Experiment #4 with pyrite particles. Severe localized attack was seen on this specimen in Experiment #4. The features of these pits are shown in Figure 20, which are similar to the pitting features detected in Experiment #1 in an H_2S solution. The profilometry of this steel specimen is shown in Figure 21 (a) and the pit with a maximum depth of 70 μm is shown in Figure 21

(b). Clearly, severe localized corrosion was detected in the presence of pyrite particles in a CO_2 solution as well, and it is believed that this localized corrosion was due to a galvanic coupling between pyrite particles and the steel.
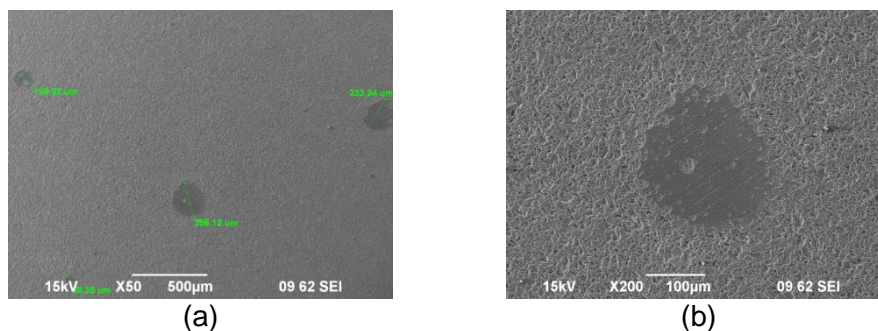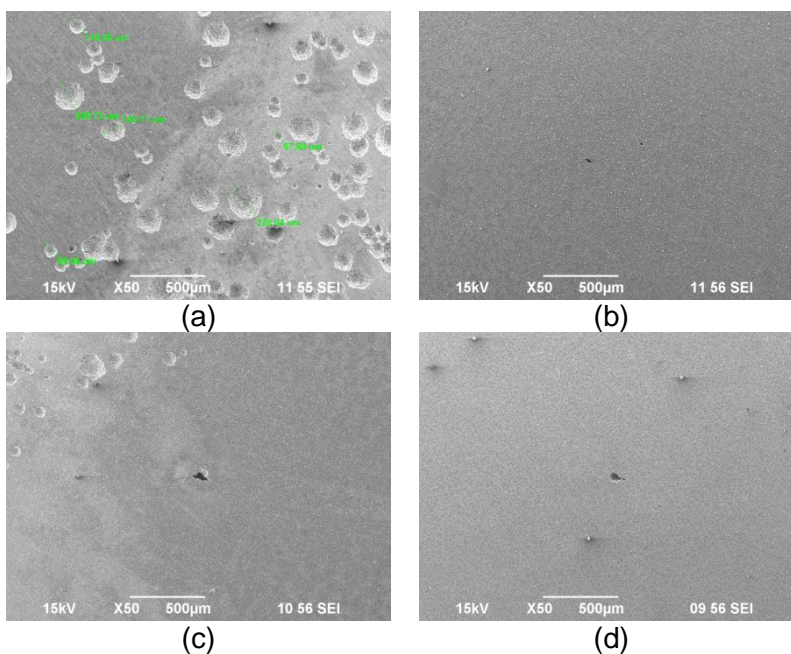

(a) (b)

Figure 18. Surface morphologies of the sample after removing the corrosion product layer using silica sand deposit in an aqueous CO_2 solution in Experiment #3: (a) 50x SEM image; (b) 200x SEM image (2 mm thick silica sand deposit layer, $pCO_2 = 0.97bar$, initial pH 4.0, T = 25 ^{o}C).

(a) (b)

(c) (d)

Figure 19. Surface morphologies of the sample after removing the corrosion product layer using pyrite particle deposit in an aqueous CO_2 solution in Experiment #4 (2 mm thick pyrite particles deposit layer, $pCO_2 = 0.97bar$, initial pH 4.0, T = 25 ^{o}C).
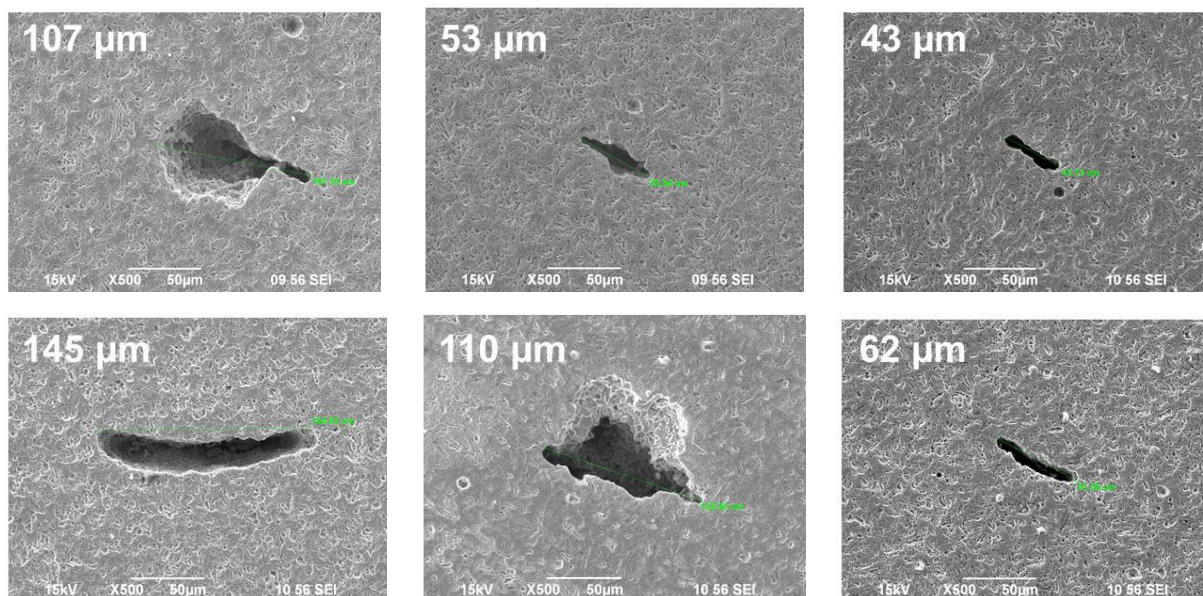
Figure 20. Locations of localized attack on the sample after removing the corrosion product layer using pyrite particle deposit in an aqueous CO_2 solution in Experiment #4 (2 mm thick pyrite particles deposit layer, pCO_2 = 0.97bar, initial pH 4.0, T = 25 ^{o}C).
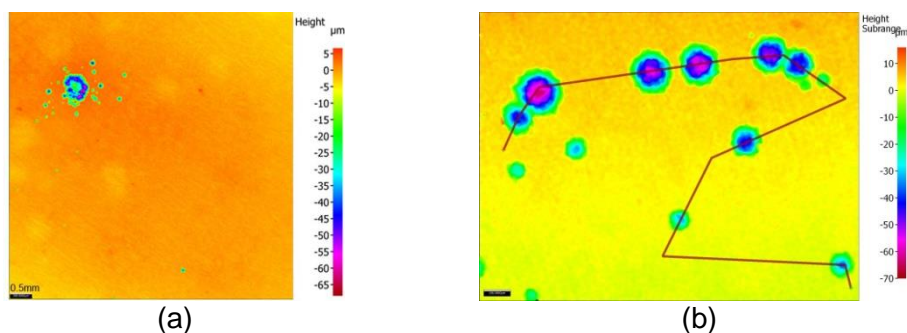

(a)   (b)

Figure 21. (a) Profilometry feature using 150 ~ 400 µm pyrite particle deposit in an aqueous CO_2 solution; (b) The maximum pit depth found on the sample in Experiment #4 (2 mm thick pyrite particles deposit layer, pCO_2 = 0.97bar, initial pH 4.0, T = 25 ^{o}C).

Figure 22 compares corrosion rates between these two experiments in an aqueous CO_2 environment. No localized corrosion was seen in the presence of silica sand. However, localized corrosion with a penetration rate of 4 mm/year was observed for Experiment #4 in the presence of pyrite particles in a CO_2 solution.
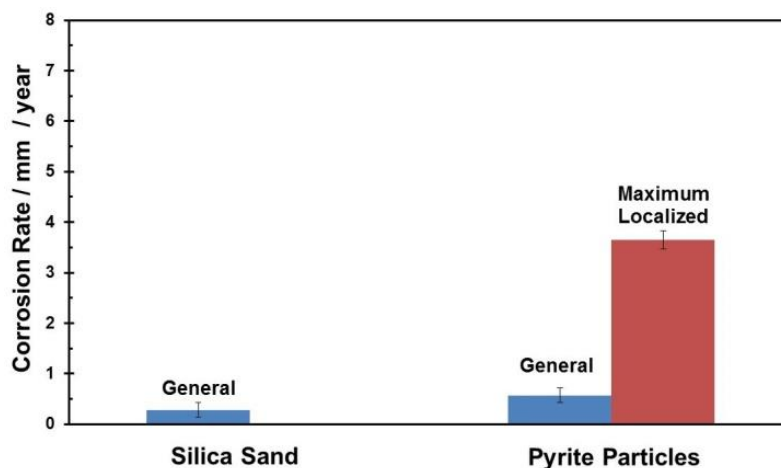
Figure 22. Comparison of corrosion rates between silica sand deposit and pyrite particle deposit in an aqueous CO_2 solution.

CONCLUSIONS

- Severe localized corrosion was observed and replicated in the presence of pyrite deposit layers in both H_2S and CO_2 dominated aqueous environments.
- The galvanic coupling between pyrite particles and steel is proven to be the dominant mechanism for this type of localized corrosion.

ACKNOWLEDGEMENTS

REFERENCES

1. J. Ning, Y. Zheng, B. Brown, D. Young, S. Nesic, *Corrosion* 73 (2017): p. 155–168.
2. J. Ning, Y. Zheng, D. Young, B. Brown, S. Nešić, CORROSION/2016, paper no. 7502, 2016.
3. A. J. Devey, Ph.D. dissertation, University College London, 2009.
4. C. Pearce, R. Pattrick, D. Vaughan, "Electrical and Magnetic Properties of Sulfides," Sulfide Mineralogy and Geochemistry, Reviews in Mineralogy and Geochemistry, Mineralogical Society of America, 61 (2006): pp. 127-180.
5. R. Schieck, A. Hartmann, S. Fiechter, R. Konenkamp, H. Wetzel, *J. Mater. Res.* 5, 7 (1990): pp. 1567-1572.
6. M. Caban-Acevedo, M. S. Faber, Y. Tan, R. J. Hamers, S. Jin, *Nano Letters* 12, 4, (2012): pp. 1977–1982.
7. P. K. Abraitis, R. A. D. Pattrick, D. J. Vaughan, *Int. J. Miner Process* 74, (2004): pp. 41–59.
8. R. C. Woollam, A. Huggins, C. Mendez, J. R. Vera, W. H. Durnie, Corrosion/2013, paper no. 2715, 2013.
9. S. M. Wilhelm and B. R. W. Hinton, "Galvanic corrosion caused by corrosion products," in Galvanic Corrosion, H. P. Hack, Ed., Philadelphia, PA: American Society for Testing and Materials, 1988, pp. 23–34.
10. S. N. Esmaeelyz and S. Nesic, *J. Electrochem. Soc.*, 164 (12) C664-C670 (2017).